ORIGINAL ARTICLE

Mechanical and microstructural characterization of Ti6Al4V lattice structures with and without solid shell manufactured via electron beam powder bed fusion

Francesco Cantaboni[1] · Davide Battini[1] · Keren Z. Hauber[2] · Paola S. Ginestra[1] · Marialaura Tocci[1] · Andrea Avanzini[1] · Elisabetta Ceretti[1] · Annalisa Pola[1]

Abstract

The topological optimization of components by means of lattice structures allows to reduce their weight avoiding a loss in the mechanical performance. Often the lattice parts are integrated in a more complex geometry, and they present an interface with a solid part.

In the present paper, the mechanical and microstructural characterization of Ti6Al4V lattice structures with body-centered cubic unit cell was carried out. Samples with and without an external solid shell were designed and produced with electron beam powder bed fusion in order to investigate the behavior of these complex structures, especially at the interface between the solid and lattice parts. The microstructure and defects were analyzed, and compression tests were performed on the samples with and without solid shell to understand the influence of the solid part and its interaction with the lattice structure. After the fracture and detachment of the shell, the same behavior for both set of samples was observed.

Finally, a finite element model was defined to better understand the mechanical behavior of the investigated structures. The nominal sample stiffness was significantly higher than the experimental one. This discrepancy can be attributed to local defects, both in terms of porosities and deviations from ideal geometry.

1 Introduction

Additive manufacturing (AM) can be successfully used to produce metallic structures. In particular, powder bed fusion (PBF) systems are in constant growth and present many advantages over traditional technologies since they allow to produce structures with complex internal shapes [1–5]. In PBF systems, both laser and electron beam sources can be used to melt the metal powder [6, 7].

In the electron beam powder bed fusion (EB-PBF) process, the electron beam locally melts the powder in a vacuum atmosphere, and the build chamber is maintained at high temperature (~ 1000 °C or above if needed) during the

manufacturing process. This allows to obtain samples and components with reduced residual stresses. On the other hand, components produced with this technology suffer from poor surface quality due to the beam energy [8].

One of the most used alloys in the industrial applications of AM is Ti6Al4V alloy, applied in several fields due to its relevant mechanical properties, high corrosion resistance, and good processability, also at high temperatures [9]. For instance, Ti6Al4V alloy is widely used for the production of biomedical implants [10]. Furthermore, Ti6Al4V alloy is used for the production of porous structures, such as scaffolds and lattice structures, needed for lightweighting and reducing the stiffness of components [2, 6, 7].

Lattice structures can be easily manufactured using EB-PBF techniques modifying the cell type and size in order to have different densities. Specifically, lattices can be applied in energy absorption applications, such as packaging and protective devices, and have potential applications in thermal systems [11]. Different studies analyzed the mechanical behavior of lattice structures by changing the density

✉ Francesco Cantaboni
  f.cantaboni@unibs.it

1 Department of Mechanical and Industrial Engineering, University of Brescia, Via Branze 38, 25123 Brescia, Italy

2 Institute of Metals, Technion City, 320003 Haifa, Israel

and cell and strut dimensions [12, 13]. It was demonstrated that the production of lattice structures with PBF technology is affected by the size, length, and orientation angle of struts [14]. Several studies on the geometry of lattice manufactured with EB-PBF are also reported in the literature. Hernández-Nava et al. [15] found that the dimensions of the struts differed from the designed one and were undersized due to the sub-optimal offset in the contour parameters. The welding process produced an oversizing of the small features when a contour around the strut diameter was applied. Suard et al. [16] demonstrated a discrepancy in size between the designed and manufactured struts which induced a decrease in the stiffness of the strut and Young's modulus in the lattices due to mismatches between CAD and as-built parts. Huang et al. [17] demonstrated that the struts of the sample were highly irregular and rough. The main contributing factor was the partially melted powder adhered to the surface which was formed during the EB-PBF process. The application of EB-PBF led to an average strut size that exceeded the designed strut size by more than 10%.

Among the different challenges in the design, production, and characterization of components containing a lattice structure, the interaction between the lattice itself and a solid surface or a bulk part represents a crucial topic. In fact, rarely purely lattice components are manufactured, but more often, the lattice is surrounded by or connected to solid walls, which can influence the mechanical behavior of the component.

In this regard, Güden et al. [18] investigated the effect of the number of cells, strut diameter, and rigid-face sheets on the compression behavior of EBM-Ti6Al4V body-centered cubic lattices. The addition of a dense layer that covered the lattice core altered the behavior of the structure compared with the lattice without a solid shell. The solid layer constrained the edge of the lattice and the fracture mode changed with and without the solid face sheets. Moreover, the mechanical properties of foam-filled tubes were investigated by Novak et al. [19]. In this study, thin-walled tubes were filled with various metal lattices. The interaction between tube and lattice structures gave a positive contribution to the energy absorption increasing the impact properties. This application is useful not only for the biomedical application but also for the automotive, marine aerospace, and railway industries. Furthermore, Xiong et al. [20] studied porous metallic scaffolds with dense core structures with different diameters to test the effectiveness in enhancing the strength of the scaffold. The tested lattice structures with dense cores exhibited mechanical features and level of porosity favorable for biomedical applications. Finally, Fu et al. [21] focused on the mechanical properties of triply periodic minimal surface shell lattices produced by micro laser powder bed fusion. The lightweight design was analyzed, and the deformation mechanisms and mechanical

properties of the shell lattices were correlated to the relative density. The deformation mechanism was highly dependent on the relative density, and the discrepancy between the design and measured values of the shell thickness was a crucial point, especially for the low density structures. These studies revealed that the addition of the solid part resulted in an increase in mechanical properties due to the higher load support than the lattice without the shell. Moreover, enhanced compression strength and energy absorption were also detected maintaining a good level of porosity of the samples. An additional example is the investigation by Dong et al. [22] into solid-lattice hybrid structures, which consist of both solid and lattice components. In this study, a specifically designed model of solid-lattice hybrid structure was introduced. The model included optimized strut thickness connected to the solid part through Boolean operations and was compared with both pure solid and pure lattice structures. The findings illustrated that the solid-lattice hybrid structure exhibited superior mechanical performance. Additionally, lattice structures are incorporated into pre-existing components to reduce weight while maintaining equivalent mechanical properties, as highlighted by Bertol et al. [23]. Moreover, Wang et al. [24] suggested a multi-scale design approach for solid-lattice hybrid structures to provide new opportunities for next-generation aerospace vehicle components, characterized by lightweight construction and high-performance improvement.

The relevant number of studies that mention the interaction between a solid and a lattice structure demonstrates the growing interest in these designs and the relative mechanical behavior. From the literature, it appears that it is crucial to analyze how the connections between the struts and the solid wall influence the behavior of these structures and how the defects are distributed. However, the solid part in the hybrid structure is usually applied above and below the lattice part (lattice sandwich structure). In the present study, the designed solid shell was applied on the lateral side of the lattice, parallel to the direction of the compression load. The shell constrains the inner lattice avoiding its free expansion under compression load. In contrast to the hybrid structures studied in the literature, the solid-lattice interface was affected by stress due to the compression load and deformation of the inner lattice part. The compression behavior of lattice with lateral-shell, and the interface solid-lattice, was investigated.

In particular, in this work, Ti6Al4V lattice structures with body-centered cubic (BCC) unit cells were designed with and without a solid shell and produced by the E-PBF process with an orientation of 90° in relation to the building platform in order to provide additional insight into the behavior of such complex structures.

The microstructural and mechanical characterization of the samples were carried out on the samples with and

without the shell. The analysis of the lattice without the solid shell was carried out for comparison to provide a better understanding of load-bearing capacity of the hybrid solid-lattice structure. Moreover, finite element model (FEM) parameters were extracted based on the mechanical tests on the lattice structures, and a numerical analysis of the mechanical performances was carried out to compare experimental and simulation results.

2 Materials and methods

2.1 Samples production

The Ti6Al4V square-based lattice structures were designed using PTC Creo parametric (CREO®). The samples were characterized by a body-centered cubic (BCC) unit cell with a length (a) of 2 mm, a volume of $2\times2\times2$ mm³, and cylindrical struts with diameter (Øs) of 500 μm, as reported in Fig. 1. For better comprehension, the junction of the oblique struts will be named node.

As reported in Fig. 1, the lattice structures were designed with and without an external solid shell. The structures are named S and NS, respectively (Fig. 1). The dimension of both sets of samples was 24 (L)×24 (L)×30 (H) mm, where L and H are the length and the height of the cube, respectively. The thickness of the shell (t) was 1 mm. The samples with and without solid shell were produced with an orientation of 90° in relation to the printing plate (plane XY), which represents the vertical direction [25]. This configuration was chosen to ensure that the growth of the four walls was perpendicular to the direction of the roller avoiding distortion of the structure.

The samples were manufactured with Ti6Al4V (grade 5) alloy powder, with particle size distribution (PSD) in the range of 40–80 μm [26], produced by GE additive®. The nominal chemical composition is reported in Table 1 [13].

Each sample was designed as a unique.STL file considering the lattice and the shell part merged. The specimens were produced by EB-PBF technology (Arcam EBM A2X, GE®, USA) with a single set of process parameters reported in Table 2. The process parameters used in the present study were selected based on a previous work of some of the authors [27]. In this paper, it is clearly demonstrated that the selected set of process parameters is optimal to produce samples with different building directions in relation to the printing plate correlated to the orientation of the struts of the lattice.
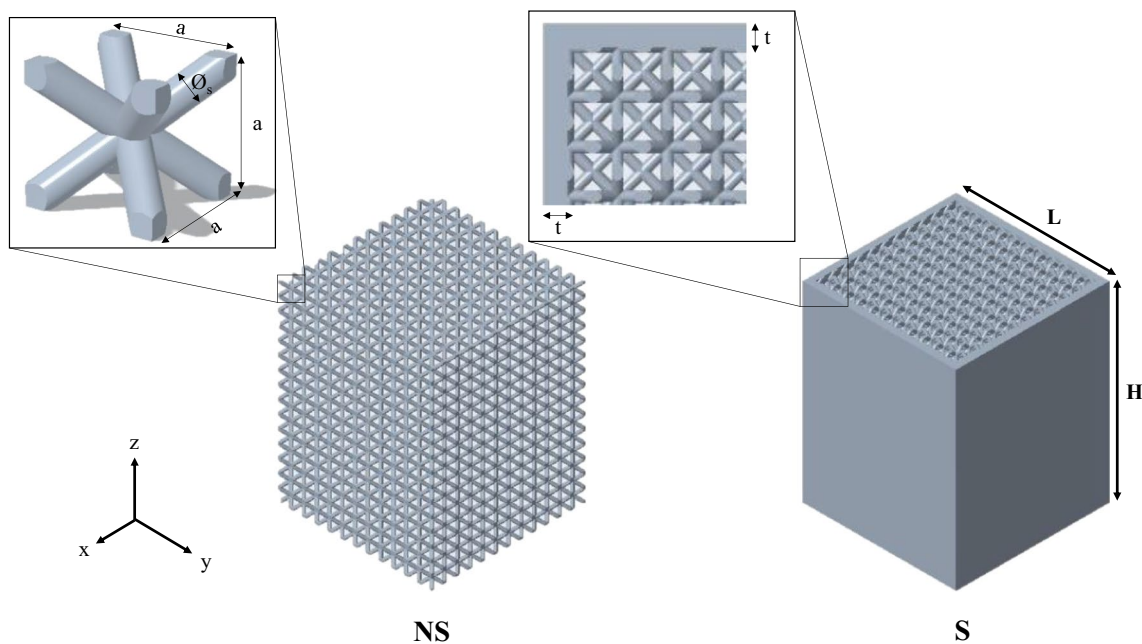

Fig. 1 Design of body-centered cubic (BCC) unit cell and design of the samples with and without solid shell (S and NS) produced with an orientation of 90° respect to the printing plate xy

Table 1 Chemical composition of Ti-6Al-4 V alloy

Ti6Al4V	Al	V	Fe	C	O	N	H	Ti
Wt min (%)	5.50	3.50	0.00	0.00	0.00	0.00	0.00	Bal
Wt max (%)	6.75	4.50	0.30	0.08	0.20	0.05	0.02	

Table 2 Process parameters of EB-PBF Arcam EBM A2X machine [27]

Process parameters	
Hatch spacing (μm)	100
Spot size (μm)	200
Layer thickness (μm)	50
Scanning speed (mm/s)	4530
Beam current (mA)	15
Max beam current (mA)	21
Focus offset (mA)	3

2.2 Samples morphology and structure

First, the size of the samples was measured by Vernier caliper to assess the repeatability of the process. In addition, the struts morphology was observed with a scanning electron microscope (SEM), LEO EVO® 40 (Carl Zeiss AG, Italy).

For the microstructural characterization, one sample for each condition was cut to observe the cross-sections parallel and normal to the building direction. Samples were mounted in acrylic resin and polished up to mirror finishing according to conventional metallographic practices. Polished samples were observed using LEICA DMI 5000 M optical microscope (Wetzlar, Germany). The diameter of the struts and the thickness of the solid shell were measured on 60 micrographs (magnification × 50), and average values and standard deviations were calculated in order to obtain reliable results. The diameter of the strut was measured as the width of the cross-section of the strut.

Image analysis was carried out on 70 micrographs (magnification × 50) with the LAS software to evaluate the porosity level of the samples. The porosity analysis was carried out on the lattice (struts and nodes) and shell separately. The porosity of the samples was estimated as the ratio of the total pores area to the total area of the cross-section of the lattice.

Selected samples were etched with Kroll's reagent for 15 s to identify the microstructure along the longitudinal and transversal directions.

After compression tests, the fracture surface was analyzed using a scanning electron microscope (SEM) (FEI Inspect S, FEI Co., USA).

2.3 Mechanical analysis

Compression tests were performed with a servo-hydraulic testing machine INSTRON 8802 (Instron, Norwood, MA, USA) equipped with a 250-kN load cell. The tests were conducted in displacement control mode at a constant crosshead speed of 2 mm/min, and the displacement was measured using the crosshead movement. The stress (σ) was calculated by dividing the force by the nominal cross-section area of the sample as a filled cube, defined as the square of length (*l*) of each square-based sample measured. The strain (ε) was

obtained by dividing the displacement by the initial height of each sample. The ultimate strength (σ_m) was identified as the maximum, and the yield stress (σ_Y) was defined as the stress at 0.2% of plastic deformation. The elastic modulus was calculated considering the linear trend of the elastic field of the stress–strain curves. Three repetitions for each sample were carried out, and the tests were considered completed when the samples reached 20% of strain, to assure uniformity of results interpretation. Moreover, the energy absorption was calculated until the first peak of stress (W_M) and until the end of the compression test (We) by Eq. 1.

$$W = \frac{1}{100} \int_0^{\varepsilon_0} \sigma d\varepsilon \tag{1}$$

W is the energy absorption per unit volume; σ is the nominal compressive stress calculated as the load over the full cross-section area, ε is the nominal strain calculated as the crosshead displacement over the initial length, and ε_0 is the upper limit of the compressive strain. The equation was divided by 100 because the strain value was defined as a percentage. In addition, the fracture and failure modes of the samples were investigated.

2.4 Finite element model

The finite element software Simulia Abaqus® was used to simulate the behavior of the lattice samples within the elastic regime. Since there is abundant evidence in the literature that FEA of lattice structures is difficult, different models were implemented, based on different assumptions regarding deviations of the real structure and testing conditions from the ideal ones. A total of six different models were realized with three geometry/material variants for the S lattice and three geometry variants for the NS lattice. One variant for each lattice type represented the stiffest condition which corresponds to the ideal lattice specimens (material constants from the powder supplier's datasheet and nominal geometry). A second variant represented lattice specimens with average stiffness, associated with average geometry size and an average Young modulus correction to account for shell porosities. A third variant represented lattice specimens with minimum stiffness, associated with minimum geometry size and maximum Young modulus correction.

Overall, the nominal Young modulus is 120 GPa, and the correction was only applied to the shell material as the porosity level of struts and nodes porosities was negligible. Since different approaches to predict a modulus correction are available, a corrected Young modulus range of 100–110 GPa for 6% porosity was gathered by considering the analytical approach from [28], the FEM approach from [29], and the experimental data on laser powder bed fusion (L-PBF) Ti6Al4V from [30, 31]. For this reason, a

Table 3 Measured dimensions of as-built S and NS lattice samples

	H (mm)	L (mm)
S	29.41 ± 0.04	23.75 ± 0.05
NS	30.13 ± 0.09	24.03 ± 0.07

Young modulus of 105 GPa was used for the shell material of the average stiffness variant, and a Young modulus of 100 GPa was used for the most compliant variant.

The current FEM model aims at estimating stiffness, and its validity is limited to the macroscopic linear-elastic response of the lattice. This choice allowed exploiting all the symmetry planes of the geometry and boundary/loading conditions, thus leading to the model of 1/8th of the cross-section and half-thickness layer (see Fig. 2). The modelling of non-linear effects is well beyond the purpose of the current finite element study as catching the full response of the compression tests would require the experimental characterization of a damage constitutive law and, possibly, the implementation of local defects, non-ideal geometry, trapped unmelted powder and the full lattice to also account for friction at lattice ends.

A Z-displacement was applied on the face highlighted in blue while the opposite face was constrained with a Z-symmetry boundary condition. Faces highlighted in red were instead constrained with a symmetry boundary condition along the tangential direction of a cylindrical coordinate system centered on the Z-axis.

3 Results and discussions

3.1 Lattice characterization

The dimensions of the manufactured struts of S and NS samples are measured and reported in Table 3.

The dimensions of the S parts are lower than the designed one as already analyzed [16]. For the NS parts, the dimensions are quite close to the designed ones. The differences between the experimental and the designed values can be attributed to the irregularities of the surfaces [26] and can be due to the suboptimal offset of contour parameters and influenced by the strut inclination angle [14, 16].

The morphology of the struts of NS samples was observed under SEM (Fig. 3). The surface appears extremely irregular, with unmelted or partially melted powder particles clearly visible on all the struts (Fig. 3a–b). The irregularity of the surface was not attributed to the samples design but to the production process. The spot of the electron beam, the residual powder adhered on the surface, and the strut orientation changed the size of the diameter as already observed in the literature [32, 33]. The SEM images of S samples are not reported for brevity's sake since they showed the same features.

The partially melted powder is more visible in Fig. 3c with an average particle size of 62 ± 17 μm, which is within the nominal range value of 40–80 μm reported on the datasheet of the Ti6Al4V alloy powder [34]. Moreover, the high variation in the thickness of the struts is particularly evident in Fig. 3c, where also a staircase-shaped profile can be observed, with gaps between layers. An evident staircase effect is typical for the EB-PBF process, leading to larger surface roughness [35]. The evident irregularity in the size of the struts will be better investigated by performing a specific dimensional analysis on the cross-section of the samples. Moreover, the surface of the struts, with the layer scanned by electron beam partially covered by the next one, is visible in Fig. 3d, as mentioned also by Zhang et al. [14].

The thickness of the solid shell for S samples and the diameter of the struts for S and NS samples were measured on three different cross-sections of the specimens, and the results are reported in Table 4.
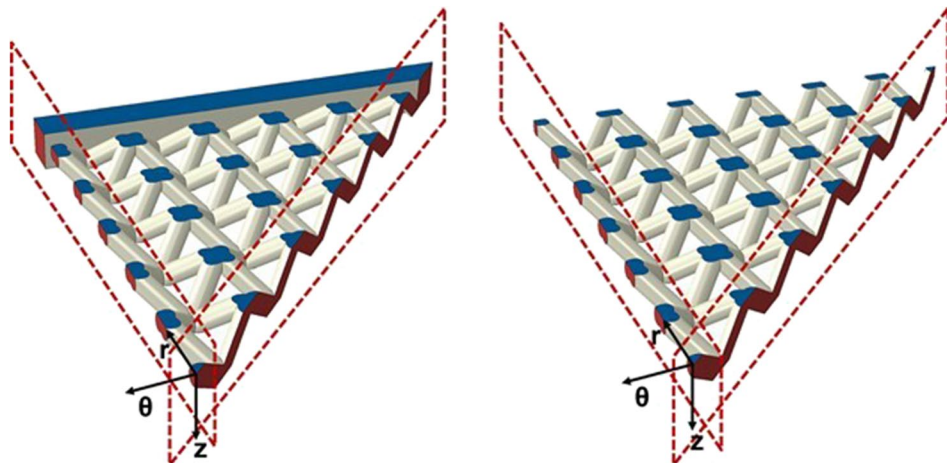

Fig. 2 FEM model of the lattice structures (nominal S on the left, nominal NS on the right)

Fig. 3 SEM images of the **a** strut and **b** node connections, **c** different melted layers, and **d** unmelted powders for NS samples
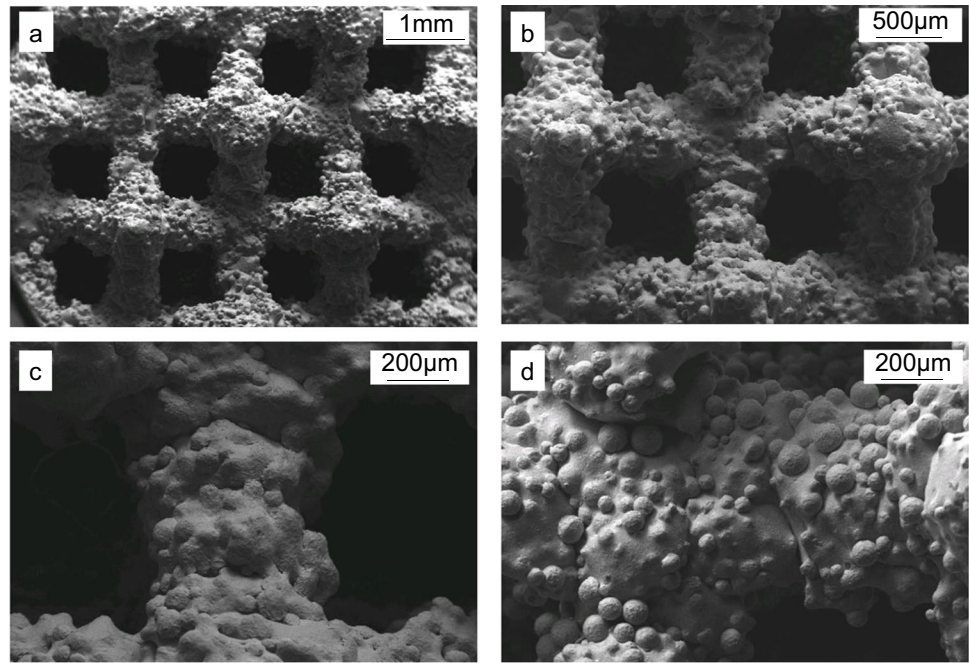

Table 4 Measured dimensions of as-built S and NS lattice samples

|	Øs (μm)	t (μm)
S	459 ± 43	608 ± 202
NS	475 ± 41	-

The struts appear extremely irregular in size, as seen by SEM analysis. The diameter of the struts for S and NS samples differs by 10% and 5% from the designed size (500 μm), respectively. The significant standard deviation detected is likely due to the inclination angle of the struts and the presence of partially melted and unmelted powder.

The thickness of the shell is lower than the designed one and shows an instability in size, demonstrated by the large standard deviation. The dimension fluctuates from a minimum of 406 μm to a maximum of 810 μm. In Fig. 4, the irregular geometry on the cross-section normal (Fig. 4a) and parallel (Fig. 4b) to the building direction is shown.

As abovementioned, the porosity of the samples was calculated using image analysis along the cross-section normal and parallel to the building direction on the solid shell and the lattice part (nodes and struts). A relatively high porosity level of 5% was detected on the shell, while a porosity level of 0.6% on the struts and nodes was measured for the S samples. A porosity value of 0.4% was detected for the struts and nodes cross-section of NS samples. The results are in accordance with porosity analysis from Suard et al. [16] and Neils et al. [36].

The reason behind the significant porosity level of the shell can be found in the process parameters, and more precisely in the contour strategy and hatch spacing used [37, 38]. Moreover, it has been decided to set the same process parameter for both lattice and shell, merging them in a unique component. In fact, large porosities can be observed in the central part of the solid shell because the strategy of the beam and the hatch spacing used for the

Fig. 4 Micrographs of the cross-section normal to the building direction of solid shell (**a**) and strut and solid shell (**b**) of S90 sample
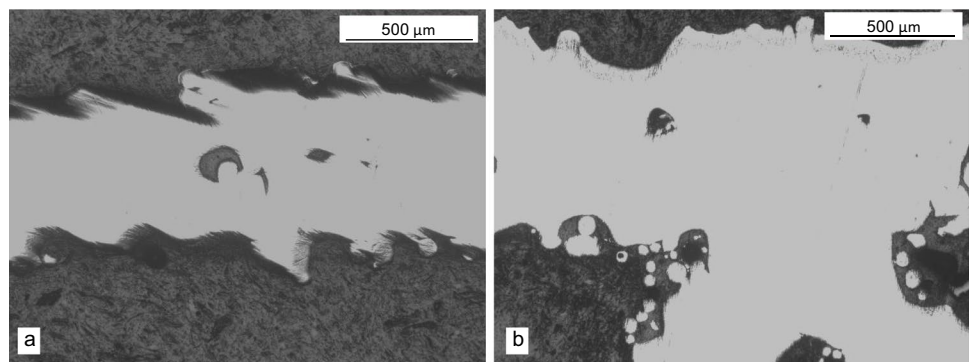
lattice part were also used for the shell. This indicates that the powder was melted on the edge of the solid shell but not in the center. The unmelted powder was detected in the central part of the shell: this resulted in the large lack-of-fusion porosities observed and reported in Fig. 4a–b, due probably to the hatching distance of the electron beam. The interface between lattice and solid part shown in Fig. 4b did not report significant defects such as porosity or geometry discrepancy. The continuity of the building was due to the same process parameters applied for both parts merging them as a single component.

3.2 Microstructure

Micrographs of NS samples are shown in Fig. 5 as representative of the microstructure of all the investigated samples. No relevant differences between the shell and lattice part of the samples are found, as well as between the S and NS samples, due to the use of the same process parameters. In general, the microstructure of Ti6Al4V alloy is composed of a α + β lamellar microstructure within the previous β columnar grains oriented along the building direction. The α lamellae are arranged in Widmanstätten structure characterized by different sizes and orientations. The mentioned microstructural features are widely reported in the literature for Ti6Al4V alloy [39, 40]. More specifically, the microstructural features due to the EB-PBF process are discussed in [35, 38].

The microstructure normal to the building direction is shown in Fig. 5a. The colony pattern of α + β lamellar structure arranged in the equiaxed microstructure can be observed. In fact, along this direction, the cross-sections of the columnar grains can be observed.

The microstructure parallel to the building direction, characterized by a columnar structure, is shown in Fig. 5b. The colony pattern of α + β lamellar structure can be observed.

Moreover, the light and dark phases identify the α and β phases, respectively, as shown in Fig. 5c. In particular, the grain boundary α layer was found around the prior β grain (Fig. 5d) [25].
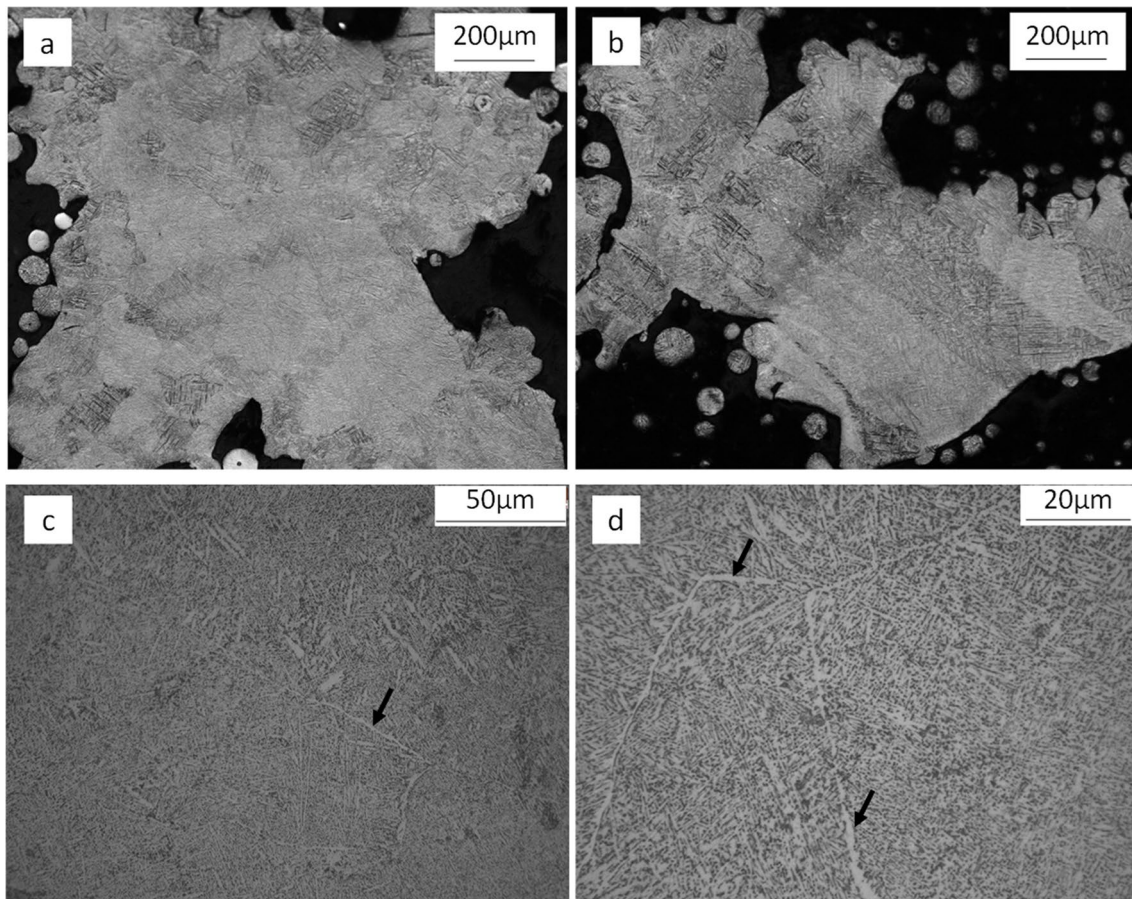

Fig. 5 Optical micrographs normal (**a**) and parallel (**b**) to the building directions of cross-sections of the NS sample. Optical micrographs parallel to the building direction (**c**, **d**). Colony pattern α + β lamellar structure divided by α phase layer (marked by black arrows) within the prior β grain boundaries

3.3 Mechanical characterization

Representative stress–strain curves resulting from the compression tests of S and NS samples are reported in Fig. 6a.

The curves are reported until 20% strain, since for higher values of strain the curves exhibited a flat plateau due to the densification of the structures. In addition, for strain above 20%, the samples with and without shell show the same behavior.

During compression tests, for both the considered designs, the stress initially increases with increasing deformation up to a maximum value (45 MPa and 155 MPa for NS and S samples, respectively). This maximum load represents the ultimate strength (σ_M). This peak in stress is related to strain values of 5–6% for both the investigated designs, even though the values of the maximum stress reached are significantly different. In fact, as reported in Table 5, the ultimate strength of NS lattices is 45 ± 2 MPa, which is approximately three times lower than 155 ± 5 MPa, demonstrated for the solid shell (S). The yield stress (σ_Y) follows the same trend and is 35 ± 2 MPa and 119 ± 5 MPa for the NS and S samples, respectively.

After the peak, a marked drop in stress is observed for S samples, while for NS samples, a smoother decrease of the stress that progressively reaches a plateau is recorded.

For NS samples, after the peak of stress, both plastic deformation and densification of the structure are noted. A stress plateau (from 8% strain) continued until the end of the test (20% strain). For S samples, the first evident drop-in stress is due to the failure of the shell structure. Afterward, for S samples, a plateau in stress between 8 and 17% strain was noted due to the densification of the structure. At 17% strain, S samples showed another drop in stress. After this, the stress–strain curves recorded for S and NS samples are comparable, indicating that in both cases, only the lattice structure is supporting the load. This is demonstrated by the observation of samples after testing, as reported in Fig. 6b–d. The S sample exhibits two different fracture modes. The first one shows a vertical fracture of the solid shell revealing the inner lattice (Fig. 6b). Moreover, a detachment of the solid shell from the lattice part along the edge and a densification of the lattice structure occur. Specifically, the solid shell under compression is detached from the inner lattice due to the lattice expansion causing the collapse of the solid shell along the vertical direction. The second type of collapse mechanism for the S samples exhibits a fracture of the shell in the central part and the detachment of the solid shell from the lattice part due to the lattice expansion (Fig. 6c). When the shell is detached from the lattice, it no longer contributes to support the structure, and this explains the severe decrease in stress recorded, as visible in Fig. 6a. The specimens tested under these conditions reached a remarkably high level of stress starting from the inner part. Therefore, the second load drop indicated the shell failure.

In addition, the orientation of the struts is crucial to understand how the lattice influences the mechanical response of the structure because they can work in compression or tensile mode giving different results. The BCC unit cell is characterized by struts inclined at 45° to the load direction. The compression load applied along the samples is divided into bending and compression components on each strut of the lattice. The lateral expansion of the lattice is due

Table 5 Results of the compression tests of S and NS samples

Properties	S	NS
σ_M (MPa)	155 ± 5	45 ± 2
σ_Y (MPa)	119 ± 5	35 ± 2
E (GPa)	6.34 ± 0.34	1.10 ± 0.03
W_M (MJ/m^3)	5.27 ± 1.03	1.83 ± 0.31
We (MJ/m^3)	9.77 ± 0.65	4.93 ± 0.15

Fig. 6 Stress–strain curves of AB samples with and without solid shell. Main failure modes after compression test on the S samples with solid shell and NS sample without solid shell
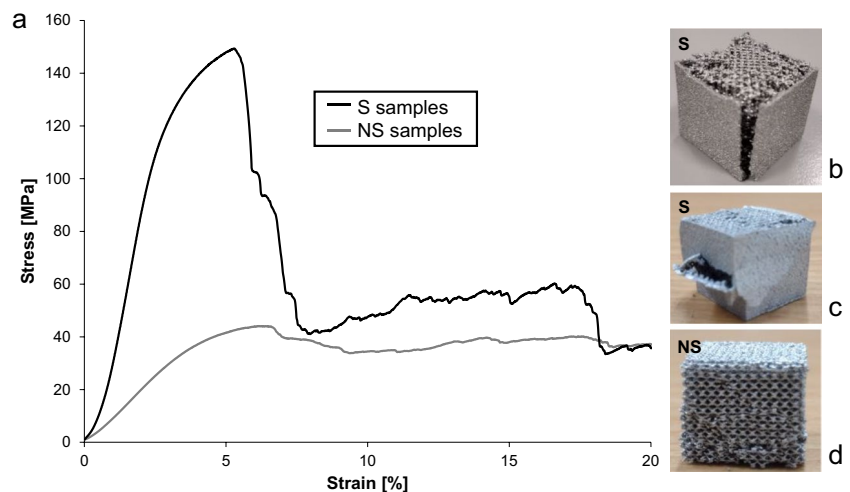
to the compression of the lattice contributing to the fracture and the detachment of the solid shell.

On the other hand, the NS samples present a 45° fracture mode (Fig. 6d) as expected for this lattice structure [25, 41, 42]. The struts, oriented along a diagonal axis, are subjected mainly to a bending load and the fracture occurs in that direction (45°) due to the geometry of the BCC unit cell. Contrarily to the S samples, the NS lattices bore the load entirely, and the bending component on the struts caused the main fracture.

The elastic modulus is calculated in the elastic region of curves shown in Fig. 6, and it is reported in Table 5. The elastic modulus of the S and NS samples is 6.34 ± 0.34 GPa and 1.10 ± 0.03 GPa, respectively. Probably, the already mentioned porosities of these structures are relevant for the elastic properties, influencing the mechanical behavior.

Moreover, the energy absorption until σ_M and until the end of the test (20% strain) is calculated and reported in Table 5. As expected, the lattices with solid shell absorb more energy when stressed and exhibit a perfect elastoplastic behavior, able to reach higher deformations. The energy absorption (We) of the lattice with the solid shell is two times higher than the one without the solid part. In fact, the presence of an external solid shell is effective in increasing the general stiffness and the energy absorption of the structure.

Moreover, the mechanical results of S samples demonstrated to bear a high load suggesting aerospace applications in addition to biomedical ones. In particular, the reduced number of defects at the interface induced high stiffness and strength in the structures, bearing the load until the lattice core expanded in lateral directions making the contribution of the shell negligible.

Considering the mechanical behavior of S samples, a detachment of the shell from the lattice part was observed, indicating that fracture is taking place at the interface. This can be enhanced from the presence of localized defects. From the microstructural analysis previously discussed (see paragraph 3.1 and 3.2), at the interface, the microstructure was not altered. In fact, the microstructure was homogeneous along the entire samples because the process parameters used were the same for both parts of the specimens. Moreover, the abrupt change in density did not affect the formation of $\alpha + \beta$ lamellar structure.

Therefore, to better understand the failure mechanism, especially the role played by the geometrical discontinuity

at the interface between shell and lattice for S samples, FEM analysis was performed on S and NS specimens.

3.4 Finite element method analysis

A first point that emerged from FEM analysis, as it can be seen from Table 6, is relative to the nominal lattice stiffness. In fact, the calculated value is much higher than the experimental measure. Specifically, the nominal lattice model predicts that ideal specimens should exhibit a stiffness more than twice that observed experimentally (a stiffness ratio of 2.25) for the NS design and over three times for the S design (a stiffness ratio of 3.42). The S design showed a larger reduction across all models, most likely due to the shell being the dominant stiffness element and being less ideal than the other lattice elements (struts and nodes). This is evident when transitioning from the nominal to the average, and further to the worst-case scenario. In fact, the average model demonstrated considerably lower stiffness, with stiffness ratios of 1.77 and 1.85 for the NS and S designs, respectively. Interestingly, the worst-case scenario values closely aligned with experimental results, underscoring the importance of Young's modulus correction and the actual dimensions of struts and shell. The resulting finite element method (FEM) moduli also closely match the values reported in [8].

Overall, the current model accounts primarily for average and homogenous effects, as it corrects the geometry in size but still represents an ideal shape of shells, struts, and nodes. Therefore, the remaining discrepancy between FEM and experimental values can be attributed to local defects, both in terms of porosities and other deviations from ideal geometry. These local defects can significantly affect the bending and shear stiffness of struts and the axial stiffness of the shell, playing a crucial role not only in lattice damage but also in the macroscopic linear-elastic behavior of the lattice. This behavior can be viewed as a complex interplay of elastic elements in series and parallel, where a local increase in elastic compliance can markedly alter the macroscopic elastic response. Therefore, adjusting the model geometry and material parameters below average values can be considered a method to account for this local stiffness deficit.

The associated stress state of the lattice structures is also shown in Fig. 7 for a total applied displacement of 0.15 mm (corresponding to 0.005 mm over the modeled thickness). As expected, the geometrical discontinuity at the interface

Table 6 Young modulus of the lattice calculated from FEM analyses of S and NS samples. Red values indicate the difference against the experimental measure

Lattice type	Young modulus of the lattice structures (GPa)			
	FEM nominal	FEM average	FEM worst case	Experimental
NS	2.48 (+125%)	1.95 (+77%)	1.32 (+20%)	1.10 ± 0.03
S	21.68 (+242%)	11.71 (+85%)	7.41 (+17%)	6.34 ± 0.38

between struts and the solid shell, known as the notch effect, served as a local stress raiser. This phenomenon is a primary factor contributing to the observed fracture behavior in NS samples, where detachment of the shell from the core lattice structure was observed.

3.5 Surface fracture analysis

Representative SEM images of the fracture surface for the investigated samples are reported in Fig. 8 for the strut (Fig. 8a–b) and shell (Fig. 8c–d). No evident differences were observed when comparing the fracture surfaces at the shell or the strut. In both cases, the fracture mechanism shown in Fig. 8 clearly reports the ductile fracture of the samples, demonstrated by the presence of dimple-like structures.

The connection between the lattice part and the solid shell was crucial because of the important variation in size and geometry. As previously shown in Fig. 6b, coarse defects were not detected on the interface due to the same process parameter set. Moreover, the fracture mechanism showed the same features on the lattice and solid shell. The detachment of the solid shell from the lattice part was due to the lattice expansion and to the geometry variation from the lattice (porous structure) to the solid part (shell).

The FEM analysis confirmed the mechanical behavior of the printed samples. The porosity was the main feature that influenced the stiffness of the samples, especially for the
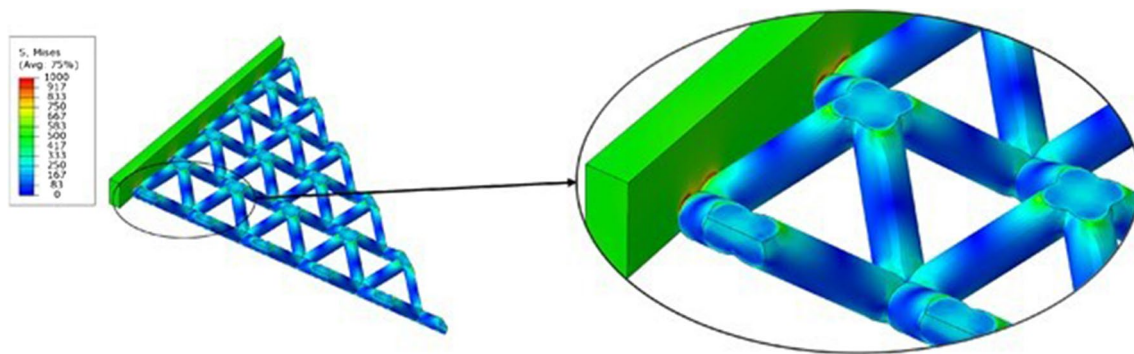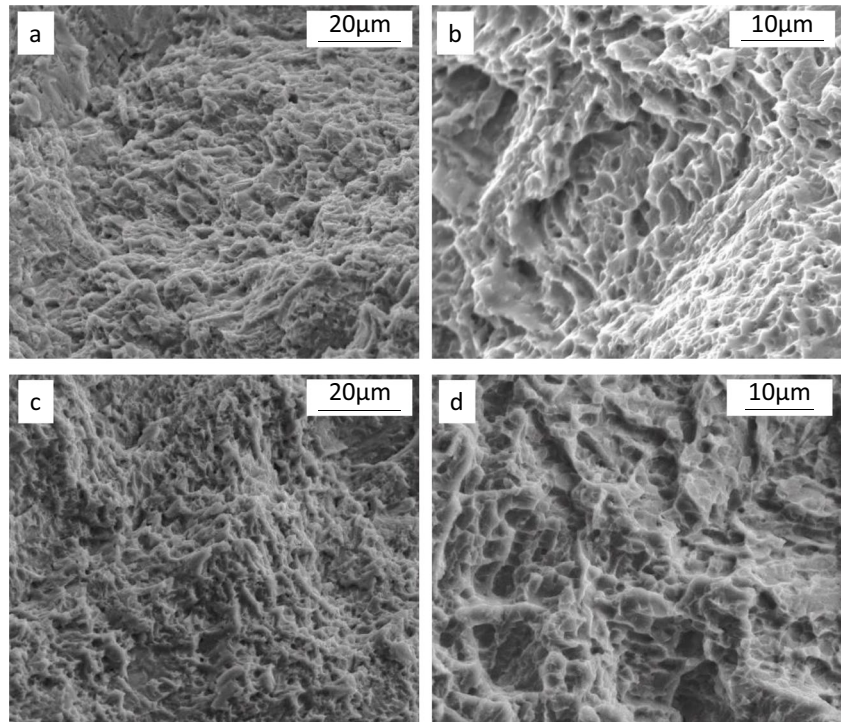

Fig. 7 Von Mises stress maps for the worst-case variants. The model was mirrored to represent 1/8 of the total lattice cross-section and a complete layer (corresponding to a thickness of 2 mm)

Fig. 8 Representative SEM images of fracture mechanism of S samples on (**a**, **b**) the strut and (**c**, **d**) shell

S samples. The high percentage (5%) of porosity localized into the solid shell, especially in the center part, made the structure less stiff than the designed one (in accordance with the stiffness of Ti6Al4V) [2, 43]. The lattice part exhibited porosity level in a range between 0.4 and 0.6%, not as influential as in the solid part.

4 Conclusions

The present work provides a combined experimental and numerical analysis to investigate the compressive response of additively fabricated Ti6Al4V lattice structures with BCC unit cell, with (S) and without (NS) solid shell. The S and NS samples were manufactured at 90° build angle to the EB-PBF printing plat e.

The main results presented in this work lead to the following conclusions:

- The process affects the morphology of the samples. In particular, the parameters of the electron beam made the solid shell irregular, probably due to a combination of the hatch spacing, the current, and the scan speed values. In fact, a relatively high porosity level of 5% was detected in the shell, while a porosity level of 0.6% of the struts and nodes cross-section was measured for both sets of samples.
- The ultimate strength of NS lattices is three times lower than that of the samples with the solid shell. The S samples absorb more energy than the NS lattice due to the presence of the solid shell. In fact, until the end of the compression test, the S samples absorb twice as much energy as the NS specimens. The presence of the solid shell results also in a higher stiffness of the samples (the S samples are 20% stiffer than the NS ones).
- The yield stress is also influenced by the solid shell. The σ_Y of S samples is 30% higher than that of the NS samples. In general, the S samples exhibit perfect elastoplastic behavior, able to reach higher deformations. The presence of an external solid shell is effective in increasing the general stiffness and the energy absorption of the structure.
- At the beginning of the tests, the solid shell of S samples mainly supports the load, and the lattice structure gives a minor contribution. After the detachment of the shell, the mechanical behavior of the S samples is the same as NS lattices, because the shell is separated from the lattice core, and it is no longer able to carry the load. In fact, from the 20% of deformation, the curves become perfectly overlapped because the shell contribution becomes negligible.
- The FEM analysis reveals that the nominal lattice stiffness should be more than twice and three times that experimentally observed for the NS and S samples,

respectively. This is mainly attributed to significant porosities and deviations from ideal geometry. The material parameters and geometry dimensions adjustments carried out for the worst-case scenario model led to a much better reproduction of the experimental stiffness. The FEM analysis for S samples also confirms that the connection between the struts and the solid shell is a critical point where high stresses are reached, leading to the detachment of the shell.
- Ductile fracture occurs for S and NS samples. In particular, S lattices exhibit first the fracture of the shell, due to the lateral expansion of the lattice and the detachment of the external shell from the lattice part. The NS lattice shows a 45° fracture as widely shown in literature. When the shell has been detached from the lattice core, the S and NS samples show the same mechanical behavior.

To summarize, it emerged that the shell provides a positive contribution needed to better support the load in terms of maximum strength and energy absorption, especially for small deformations. On the other hand, more significant deformations of the structure lead to a concentration of stresses at the interface between the struts and the solid shell, resulting in the detachment of the shell itself. This has to be taken into account to design lattice structures properly and to exploit their potential, making it useful for many industrial applications. Considering the biomedical field, the structure of S samples can provide interconnected pores that facilitate tissue growth and development in the inner part and a solid shell that can support the whole structure. However, observing the results of the compression tests, the detachment of the shell must be analyzed for the validation of load-bearing application [44]. The results obtained in the present study can help to better understand the behavior of these structures as a function of the applied load.

Considering the results obtained for the S samples from the compression tests, the studied structures could be also used as space fillers or conformal parts for lightweight engineering, shock absorption, or heat exchangers in aerospace [45].

The key point is to find the best compromise between lightweight and reliability based on the application.

Declarations

Competing interests The authors declare no competing interests.

References

1. Sepe R, De Luca A, Giannella V, Borrelli R, Franchitti S, Di Caprio F et al (2022) Influence of dimension, building position, and orientation on mechanical properties of EBM lattice Ti6Al4V trusses. Int J Adv Manuf Technol 122:3183–3198. https://doi.org/10.1007/s00170-022-10051-3

2. Grazia Guerra M, Lafirenza M, Errico V, Angelastro A (2023) In-process dimensional and geometrical characterization of laser-powder bed fusion lattice structures through high-resolution optical tomography. Opt Laser Technol 162:109252. https://doi.org/10.1016/j.optlastec.2023.109252

3. Lin Y, Shi W, Li J, Liu Y, Liu S, Li J (2023) Evaluation of mechanical properties of Ti–6Al–4V BCC lattice structure with different density gradient variations prepared by L-PBF. Mater Sci Eng A 872:144986. https://doi.org/10.1016/j.msea.2023.144986

4. Sajjad R, Chauhdary ST, Anwar MT, Zahid A, Khosa AA, Imran M et al (2023) A review of 4D printing – technologies, shape shifting, smart polymer based materials, and biomedical applications. Adv Ind Eng Polym Res. https://doi.org/10.1016/j.aiepr.2023.08.002

5. Masood Arif Bukhari S, Husnain N, Arsalan Siddiqui F, Tuoqeer Anwar M, Abbas Khosa A, Imran M, et al. (2023) Effect of laser surface remelting on microstructure, mechanical properties and tribological properties of metals and alloys: a review. Opt Laser Technol 165. https://doi.org/10.1016/j.optlastec.2023.109588

6. Liu S, Shin YC (2019) Additive manufacturing of Ti6Al4V alloy: a review. Mater Des 164:107552. https://doi.org/10.1016/j.matdes.2018.107552

7. Lazar PJL, Subramanian J, Manickam M, Selvaraj VK (2023) Imperfections and computational modeling of lattice structures developed through powder bed fusion - a short review. Mater Today Proc 2023:2–7. https://doi.org/10.1016/j.matpr.2023.02.269

8. Cheng XY, Li SJ, Murr LE, Zhang ZB, Hao YL, Yang R et al (2012) Compression deformation behavior of Ti-6Al-4V alloy with cellular structures fabricated by electron beam melting. J Mech Behav Biomed Mater 16:153–162. https://doi.org/10.1016/j.jmbbm.2012.10.005

9. Onuike B, Bandyopadhyay A (2018) Additive manufacturing of Inconel 718 – Ti6Al4V bimetallic structures. Addit Manuf 22:844–851. https://doi.org/10.1016/j.addma.2018.06.025

10. Sidambe AT (2014) Biocompatibility of advanced manufactured titanium implants-a review. Materials 7:8168–8188. https://doi.org/10.3390/ma7128168

11. Sajjad U, RehmanTur Ali M, Park CW, Yan WM (2022) Manufacturing and potential applications of lattice structures in thermal systems: a comprehensive review of recent advances. Int J Heat Mass Transf 198:123352. https://doi.org/10.1016/j.ijheatmasstransfer.2022.123352

12. Pathania A, Subramaniyan AK, Nagesha BK (2022) Influence of post-heat treatments on microstructural and mechanical properties of LPBF-processed Ti6Al4V alloy. Prog Addit Manuf 7:1323–1343. https://doi.org/10.1007/s40964-022-00306-6

13. Popov VV, Muller-Kamskii G, Kovalevsky A, Dzhenzhera G, Strokin E, Kolomiets A et al (2018) Design and 3D-printing of titanium bone implants: brief review of approach and clinical cases. Biomed Eng Lett 8:337–344. https://doi.org/10.1007/s13534-018-0080-5

14. Zhang XZ, Tang HP, Wang J, Jia L, Fan YX, Leary M et al (2022) Additive manufacturing of intricate lattice materials: ensuring robust strut additive continuity to realize the design potential. Addit Manuf 58:103022. https://doi.org/10.1016/j.addma.2022.103022

15. Hernández-Nava E, Smith CJ, Derguti F, Tammas-Williams S, Leonard F, Withers PJ et al (2016) The effect of defects on the mechanical response of Ti-6Al-4V cubic lattice structures fabricated by electron beam melting. Acta Mater 108:279–292. https://doi.org/10.1016/j.actamat.2016.02.029

16. Suard M, Martin G, Lhuissier P, Dendievel R, Vignat F, Blandin JJ et al (2015) Mechanical equivalent diameter of single struts for the stiffness prediction of lattice structures produced by electron beam melting. Addit Manuf 8:124–131. https://doi.org/10.1016/j.addma.2015.10.002

17. Huang Y, Wan ARO, Schmidt K, Sefont P, Singamneni S, Chen ZW (2023) Effects of cell orientation on compressive behaviour of electron beam powder bed fusion Ti6Al4V lattice structures. Mater Today Proc 2023:4. https://doi.org/10.1016/j.matpr.2023.04.522

18. Güden M, Alpkaya AT, Hamat BA, Hızlı B, Taşdemirci A, Tanrıkulu AA et al (2022) The quasi-static crush response of electron-beam-melt Ti6Al4V body-centred-cubic lattices: the effect of the number of cells, strut diameter and face sheet. Strain 58:1–20. https://doi.org/10.1111/str.12411

19. Novak N, Kytyr D, Rada V, Doktor T, Al-Ketan O, Rowshan R et al (2022) Compression behaviour of TPMS-filled stainless steel tubes. Mater Sci Eng A 852:143680. https://doi.org/10.1016/j.msea.2022.143680

20. Xiong Y, Wang W, Gao R, Zhang H, Dong L, Qin J et al (2020) Fatigue behavior and osseointegration of porous Ti-6Al-4V scaffolds with dense core for dental application. Mater Des 195:108994. https://doi.org/10.1016/j.matdes.2020.108994

21. Fu J, Ding J, Qu S, Zhang L, Wang MY, Fu MW, et al. (2022) Improved light-weighting potential of SS316L triply periodic minimal surface shell lattices by micro laser powder bed fusion. Mater Des 222. https://doi.org/10.1016/j.matdes.2022.111018

22. Dong G, Tang Y, Li D, Zhao YF (2020) Design and optimization of solid lattice hybrid structures fabricated by additive manufacturing. Addit Manuf 33:101116. https://doi.org/10.1016/j.addma.2020.101116

23. Bertol LS, Júnior WK, da Silva FP, Aumund-Kopp C (2010) Medical design: direct metal laser sintering of Ti-6Al-4V. Mater Des 31:3982–3988. https://doi.org/10.1016/j.matdes.2010.02.050

24. Wang C, Zhu J, Wu M, Hou J, Zhou H, Meng L et al (2021) Multi-scale design and optimization for solid-lattice hybrid structures and their application to aerospace vehicle components. Chin J Aeronaut 34:386–398. https://doi.org/10.1016/j.cja.2020.08.015

25. Cantaboni F, Ginestra PS, Tocci M, Avanzini A, Ceretti E, Pola A (2022) Compressive behavior of Co-Cr-Mo radially graded porous structures under as-built and heat-treated conditions. Frattura Ed Integrita Strutturale 16:490–504. https://doi.org/10.3221/IGF-ESIS.62.33

26. Parthasarathy J, Starly B, Raman S, Christensen A (2010) Mechanical evaluation of porous titanium (Ti6Al4V) structures with electron beam melting (EBM). J Mech Behav Biomed Mater 3:249–259. https://doi.org/10.1016/j.jmbbm.2009.10.006

27. Ginestra P, Ferraro RM, Zohar-Hauber K, Abeni A, Giliani S, Ceretti E (2020) Selective laser melting and electron beam melting of Ti6Al4V for orthopedic applications: a comparative study on the applied building direction. Materials 13:1–23. https://doi.org/10.3390/ma13235584

28. Roberts AP, Garboczi EJ (2000) Elastic properties of model porous ceramics. J Am Ceram Soc 83:3041–3048. https://doi.org/10.1111/j.1151-2916.2000.tb01680.x

29. Morrissey LS, Nakhla S (2018) A finite element model to predict the effect of porosity on elastic modulus in low-porosity materials. Metall Mater Trans A Phys Metall Mater Sci 49:2622–2630. https://doi.org/10.1007/s11661-018-4623-2

30. Kan WH, Gao M, Zhang X, Liang E, Chiu NSL, Lim CVS et al (2022) The influence of porosity on Ti-6Al-4V parts fabricated by laser powder bed fusion in the pursuit of process efficiency. Int J Adv Manuf Technol 119:5417–5438. https://doi.org/10.1007/s00170-021-08374-8

31. Montalbano T, Briggs BN, Waterman JL, Nimer S, Peitsch C, Sopcisak J et al (2021) Uncovering the coupled impact of defect morphology and microstructure on the tensile behavior of Ti-6Al-4V fabricated via laser powder bed fusion. J Mater Process Technol 294:117113. https://doi.org/10.1016/j.jmatprotec.2021.117113

32. Persenot T, Burr A, Martin G, Buffiere JY, Dendievel R, Maire E (2019) Effect of build orientation on the fatigue properties of as-built electron beam melted Ti-6Al-4V alloy. Int J Fatigue 118:65–76. https://doi.org/10.1016/j.ijfatigue.2018.08.006

33. Bellini C, Borrelli R, Di Caprio F, Di Cocco V, Franchitti S, Iacoviello F et al (2023) An innovative method to analyse the geometrical accuracy of Ti6Al4V octet-truss lattice structures. Materials 16:2372. https://doi.org/10.3390/ma16062372

34. Kirchner A, Klöden B, Weißgärber T, Kieback B. (2016) Powders for additive manufacturing Proceedings of the World PM2016 – AM – Powder Characteristics Congress and Exhibition, Hamburg, Germany

35. Rafi HK, Karthik NV, Gong H, Starr TL, Stucker BE (2013) Microstructures and mechanical properties of Ti6Al4V parts fabricated by selective laser melting and electron beam melting. J Mater Eng Perform 22:3872–3883. https://doi.org/10.1007/s11665-013-0658-0

36. Neils A, Dong L, Wadley H (2022) The small-scale limits of electron beam melt additive manufactured Ti-6Al-4V octet-truss lattices. AIP Adv 12. https://doi.org/10.1063/5.0094155

37. Cao X, Carter LN, Villapún VM, Cantaboni F, De Sio G, Lowther M et al (2022) Optimisation of single contour strategy in selective laser melting of Ti-6Al-4V lattices. Rapid Prototyp J 28:907–915. https://doi.org/10.1108/RPJ-04-2021-0103

38. Everhart W, Dinardo J, Barr C (2017) The effect of scan length on the structure and mechanical properties of electron beam-melted Ti-6Al-4V. Metall Mater Trans A Phys Metall Mater Sci 48:697–705. https://doi.org/10.1007/s11661-016-3866-z

39. Collins PC, Welk B, Searles T, Tiley J, Russ JC, Fraser HL (2009) Development of methods for the quantification of microstructural features in α + β-processed α/β titanium alloys. Mater Sci Eng A 508:174–182. https://doi.org/10.1016/j.msea.2008.12.038

40. Tiley J, Searles T, Lee E, Kar S, Banerjee R, Russ JC et al (2004) Quantification of microstructural features in α/β titanium alloys. Mater Sci Eng A 372:191–198. https://doi.org/10.1016/j.msea.2003.12.008

41. Distefano F, Guglielmino E, Mineo R, Epasto G (2022) Mechanical and morphological characterization of BCC - derived unit cells for biomedical devices. Procedia Structural Integrity 41:470–485. https://doi.org/10.1016/j.prostr.2022.05.053

42. Sokollu B, Gulcan O, Konukseven EI (2022) Mechanical properties comparison of strut-based and triply periodic minimal surface lattice structures produced by electron beam melting. Addit Manuf 60:103199. https://doi.org/10.1016/j.addma.2022.103199

43. Hrabe N, Quinn T (2013) Effects of processing on microstructure and mechanical properties of a titanium alloy (Ti-6Al-4V) fabricated using electron beam melting (EBM), part 1: Distance from build plate and part size. Mater Sci Eng A 573:264–270. https://doi.org/10.1016/j.msea.2013.02.064

44. Kladovasilakis N, Tsongas K, Tzetzis D (2020) Finite element analysis of orthopedic hip implant with functionally graded bioinspired lattice structures. Biomimetics 5. https://doi.org/10.3390/BIOMIMETICS5030044

45. Bici M, Brischetto S, Campana F, Ferro CG, Seclì C, Varetti S, et al. (2018) Development of a multifunctional panel for aerospace use through SLM additive manufacturing. Procedia CIRP, vol. 67, Elsevier B.V. 215–20. https://doi.org/10.1016/j.procir.2017.12.202